Anomalous strain relaxation and its impact on the valence-driven spin-state/metal-insulator transition in epitaxial math xmlns="http://www.w3.org/1998/Math/MathML">mrow>msub>mrow>mo>(/mo>mrow>msub>mi>Pr/mi>mrow>mn>1/mn>mtext>−/mtext>mi>y/mi>/mrow>/msub>msub>mi mathvariant="normal">Y/mi>mi>y/mi>/msub>/mrow>mo>)/mo>/mrow>mrow>mn>1/mn>mtext>−/mtext>mi>x/mi>/mrow>/msub>msub>mi>Ca/mi>mi>x/mi>/msub>mi>Co/mi>msub>mi mathvariant="normal">O/mi>mrow>mn>3/mn>mtext>−/mtext>mi>δ/mi>/mrow>/msub>/mrow>/math>

John E. Dewey, Supriya Ghosh, Vipul Chaturvedi, William M. Postiglione, Lucca Figari, Andrew Jacobson, Caroline Korostynski, Timothy R. Charlton, K. Andre Mkhoyan, and Chris Leighton

Phys. Rev. Materials **7**, 024415 — Published 22 February 2023

DOI: 10.1103/PhysRevMaterials.7.024415

Revised version resubmitted to *Physical Review Materials* on 1/31/2023

Anomalous Strain Relaxation and its Impact on the Valence-Driven Spin-State/Metal-Insulator Transition in Epitaxial $(Pr_{1-y}Y_y)_{1-x}Ca_xCoO_{3-\delta}$

John E. Dewey[1], Supriya Ghosh[1], Vipul Chaturvedi[1], William M. Postiglione[1], Lucca Figari[1], Andrew Jacobson[1], Caroline Korostynski[1], Timothy R. Charlton[2], K. Andre Mkhoyan[1], and Chris Leighton[1]*

[1]*Department of Chemical Engineering and Materials Science, University of Minnesota, Minneapolis, Minnesota 55455, USA*

[2]*Neutron Scattering Division, Oak Ridge National Laboratory, Oak Ridge, TN 37831, USA*

ABSTRACT: Pr-based cobaltites exhibit extraordinary phenomena where abrupt valence shifts trigger coupled structural/spin-state/metal-insulator transitions. Recent work achieved strain control of these phenomena in thin films, with epitaxial compression even stabilizing *room-temperature* transitions. Here, we study the thickness dependence of these effects in the model system compressively-strained $YAlO_3$(101)/$(Pr_{0.85}Y_{0.15})_{0.7}Ca_{0.3}CoO_{3-\delta}$(001). Transport data reveal highly unusual behavior where thicker films exhibit *two* transitions: one at the fully-strained temperature (~245 K) and one near bulk (~135 K). High-resolution X-ray diffraction confirms that this is due to anomalous strain relaxation where, immediately above the critical thickness (~30 nm), a film region with near-bulk lattice parameter coexists with a fully-strained region. Scanning transmission electron microscopy then reveals striking images where periodic arrays of dislocations occur in the film interior, rather than at the film/substrate interface, seeding accompanying lateral modulations in chemical doping. The unusual transport is thus a direct consequence of anomalous strain relaxation, which we discuss in detail. Intriguing behavior also arises in the ultrathin limit, where temperature-dependent transport and X-ray data reveal gradual suppression of the amplitude of the structural/metal-insulator transition, but with no change in

transition temperature, which we ascribe to effects of disorder in the presence of symmetry matching between the film and substrate. These results establish a new strain relaxation mechanism in perovskite oxide films (likely relevant to other systems), and further elucidate the sensitive strain response of these fascinating and potentially useful valence/structural/spin-state/metal-insulator transitions.

*Corresponding author email: leighton@umn.edu

I. INTRODUCTION

Cobalt-based perovskite and perovskite-related oxides have long been known to exhibit fascinating thermally-driven spin-state crossovers. $LaCoO_3$ is perhaps the archetype, where the d^6 Co^{3+} ions adopt a $t_{2g}^6e_g^0$ (S = 0) configuration at zero temperature (T), due to a crystal field splitting that slightly outweighs the intra-atomic Hund's rule exchange energy [1–8]. This energetic balance is so delicate, however, that occupation of e_g orbitals commences at only ~30 K, inducing thermally-excited finite-spin states and paramagnetism, which have been intensively studied [1–8]. Also now well understood, hole doping of $LaCoO_3$ (*e.g.*, with Sr) generates Co^{4+} ions, finite spin states, and, eventually, ferromagnetism (*e.g.*, [9–11]). More recently, Pr-containing perovskite cobaltites have been understood to add a new dimension to these spin-state phenomena, through abrupt spin-state *transitions*, accompanied by coupled structural and metal-insulator transitions (MITs). This remarkable phenomenon was initially discovered in $Pr_{0.5}Ca_{0.5}CoO_{3-\delta}$ (PCCO), where, at ~90 K, an unusual first-order isomorphic structural transformation takes place, where the *Pnma* cell volume decreases by ~2% on cooling, accompanied by a spin-state transition on the Co^{3+} ions, and an MIT [12,13].

The interest in the above phenomenon was further increased by the realization that it is driven by an unusual mechanism, specifically a first-order Pr *valence transition* [14–17]. As now confirmed by multiple techniques, the typical Pr^{3+} ions in PCCO and related materials abruptly shift towards Pr^{4+} on cooling through the valence transition temperature (T_{vt}), triggering a charge-balancing decrease of the mean Co valence and effective doping, thus driving spin-state and metal-insulator transitions [14–25]. This is possible because Pr is essentially the only rare-earth (RE) ion in the $RECoO_3$ series with 4*f* electronic states near the Fermi level [26,27]. Model density-functional theory calculations on PCCO in fact reproduce the temperature-dependent ionization of Pr *via* the experimentally observed cell volume collapse [14]. Many open questions remain, however, including the origin of the structural transition, the issue of which (if any) of the several coupled factors primarily drives the transition, and the relation to other known RE valence anomalies, which are of broad interest. The latter include the well-known anomalous valence tendencies of Eu [28], the fact that $PrBa_2Cu_3O_{7-\delta}$ is the sole non-superconducting member of the $REBa_2Cu_3O_{7-\delta}$ series (which is insulating due to Pr-O hybridization) [29,30], the unusual role played by Pr-O bonding in $Pr_{0.5}Sr_{0.5}CoO_{3-\delta}$ [31], and the likely related *T*-dependent valence transitions in compounds such as SmS [32].

While the above is fascinating, and realizes potentially useful transitions in RE and Co valence, coupled to structural/spin-state/metal-insulator transitions, it must be emphasized that in bulk Pr cobaltites these are cryogenic phenomena. The T_{vt} of 90 K in PCCO [12] can be increased by partial substitution of smaller-radii ions for Pr (*e.g.*, Y, Tb, Sm, and Gd [19–22,25,33–36]), *i.e.*, by favoring the low-*T* collapsed cell volume state with chemical pressure, but solubility limits and oxygen vacancy (V_O) formation limit this approach [22,25,34]. T_{vt} reaches ~135 K, for example, in $(Pr_{0.85}Y_{0.15})_{0.7}Ca_{0.3}CoO_{3-\delta}$ [25], a composition we hereafter denote "PYCCO". Our recent work

changed this *status quo* through the first full study of the tuning of the PYCCO model system *via* heteroepitaxial strain [37]. Depositing ~10-nm-thick (25-30 unit cell (u.c.)) epitaxial PYCCO films on a range of substrates (imposing from -2.1% strain (compressive) to +2.3% strain (tensile)), led to complete control over the electronic ground state, from nonmagnetic insulator under compression to ferromagnetic metal under tension [37]. Most significantly, T_{vt} increased rapidly with compressive strain, reaching 245 K in $YAlO_3$(101)/$(Pr_{0.85}Y_{0.15})_{0.7}Ca_{0.3}CoO_{3-\delta}$ and 291 K in $YAlO_3$(101)/$(Pr_{0.75}Y_{0.25})_{0.7}Ca_{0.3}CoO_{3-\delta}$ (at approximately -2% strain) [37]. This constitutes stabilization of a new structural/spin-state/metal-insulator transition system to ambient temperature, perhaps more importantly affording room-temperature control over a valence transition in a strain-tuned perovskite oxide, with broad implications, including for device applications [37].

Significantly, the above study focused almost exclusively on ~10-nm-thick (25-30 u.c.) PYCCO films, in the fully-strained, pseudomorphic regime [37]. Studying the thickness (t) dependence of these phenomena in this model system would be of clear interest, however, particularly on the ~2% compressive $YAlO_3$ (YAO) substrate that generates the largest T_{vt} [37]. Probing the evolution of the valence/structural/spin-state/metal-insulator transition with strain relaxation at higher t could enable quasi-continuous variation of the cell volume, for example, as opposed to the discrete strains imposed by pseudomorphic heteroepitaxy on various substrates [38–41]. Conversely, probing PYCCO films in the ultrathin limit would also be of interest, due to the wealth of interesting phenomena known to arise in perovskite oxides in this regime, including dead-layer formation [42–44], dimensional confinement [42,45,46], and effects of interfaces/surfaces on structural transitions [47].

Here, we thus present a *t*-dependent study of YAO/PYCCO films (2.1% compressive strain), focusing on the most extensively investigated $(Pr_{0.85}Y_{0.15})_{0.7}Ca_{0.3}CoO_{3-\delta}$ composition [20–22,25,34]. Epitaxial growth is combined with high-resolution X-ray diffraction (HRXRD) (including reciprocal space maps (RSMs)), grazing-incidence X-ray reflectivity (GIXR), atomic force microscopy (AFM), scanning transmission electron microscopy (STEM) with energy-dispersive X-ray spectroscopy (EDX), and *T*-dependent transport and HRXRD, to provide a detailed view. Transport measurements reveal unusual behavior, where, above a critical thickness (t_{crit}) of ~30 nm, *two* transitions occur, one at the T_{vt} of fully-strained films (~245 K) and one close to bulk T_{vt} (~135 K). HRXRD confirms that this is due to anomalous strain relaxation, where, immediately above t_{crit}, PYCCO films exhibit fully-strained regions coexisting with near-fully-relaxed regions. STEM imaging reveals that this is associated with a periodic array of dislocations occurring ~20 nm from the film/substrate interface, with accompanying lateral chemical doping modulations, establishing an unusual strain relaxation mechanism. Similarly interesting phenomena occur in the low *t* limit (below ~4 nm (~10 u.c.)), where the structural and metal-insulator transitions are progressively suppressed in amplitude, but with no variation in T_{vt}, which we ascribe to effects of disorder in the presence of symmetry matching between the film and substrate. This work thus significantly elucidates thickness and strain effects in this new ambient-temperature valence transition system, additionally uncovering a new strain relaxation mechanism in perovskite oxides, with broad potential relevance.

II. EXPERIMENTAL DETAILS

Polycrystalline $(Pr_{0.85}Y_{0.15})_{0.7}Ca_{0.3}CoO_{3-\delta}$ sputtering targets (2" diameter) were synthesized by solid-state reaction, cold pressing, and sintering of stoichiometric mixtures of Pr_6O_{11}, Y_2O_3,

$CaCO_3$, and Co_3O_4 powders, as reported previously [25,37]. These targets were then used for high-pressure-oxygen sputter deposition of PYCCO films between 1.8 nm (~5 u.c.) and 150 nm (~390 u.c.) thickness, at similar conditions to prior work on $La_{1-x}Sr_xCoO_{3-\delta}$ [48–50]. Briefly, YAO(101) substrates were annealed at 900 °C in 0.45 Torr of flowing ultrahigh-purity O_2 (99.998%) for 15 mins prior to growth. Deposition then took place at 600 °C substrate temperature, ~30 W of DC sputter power, and 1.4 Torr of flowing O_2, yielding ~4.1 Å min^{-1} growth rates; post growth, the films were cooled to ambient temperature in 600 Torr of O_2 at ~15 °C/min.

Film thicknesses, densities, and roughnesses were determined by GIXR using a Rigaku SmartLab XE diffractometer with Cu K_α (λ = 1.5406 Å) radiation. GenX software [51] was used to fit X-Ray reflectivity data, enabling extraction of scattering length density depth profiles. Surface morphology and roughness were additionally studied by AFM using a Bruker Nanoscope V Multimode 8 in contact mode. Film microstructures and lattice parameters were probed by HRXRD, in specular and reciprocal space mapping modes, in a Rigaku SmartLab XE. For *T*-dependent measurements (130-330 K), the Rigaku SmartLab XE was equipped with an Anton Paar DCS 500 graphite-dome cooling stage and liquid-N_2-flow cryocooler. Cross-section samples for STEM studies were prepared with an FEI Helios Nanolab G4 dual-beam focused ion beam (FIB) system. Samples were first coated with amorphous carbon prior to sectioning in the FIB to prevent damage on exposure to the ion beam. Thinning of the cross-section was done using a 30 keV Ga ion beam followed by a final 2 keV ion beam shower to remove damaged and amorphous surface layers. High-angle annular dark field (HAADF) STEM imaging and EDX spectroscopy were performed on an aberration-corrected FEI Titan G2 60-300 (S)TEM, equipped with a CEOS DCOR probe corrector and a Super-X EDX spectrometer. The microscope was operated at 200 keV with a probe current of 140 pA. A probe convergence angle of 25.5 mrad with detector inner

and outer angles of 55 and 200 mrad respectively were used for HAADF-STEM. STEM-EDX elemental maps were acquired using the Bruker Esprit software with live drift correction. DC electronic transport measurements were performed in a Quantum Design Physical Property Measurement System from 5-300 K, using a Keithley 2400 source-measure unit. A four-terminal van der Pauw geometry was employed, with either In or sputtered Mg/Pt contacts, carefully selecting excitation currents to avoid non-ohmicity and/or self-heating.

III. RESULTS AND DISCUSSION

III.A THICKNESS-DEPENDENT TRANSPORT PROPERTIES

We focus first, in Fig. 1, on the T-dependent electrical resistivity (ρ) of YAO/PYCCO films as a function of t. For clarity, this is split into $t \geq 9$ nm and $t \leq 9$ nm regimes in Figs. 1(a,c) and Figs. 1(b,d), respectively. For reference, both Figs. 1(a) and 1(b) also show the behavior of bulk polycrystalline PYCCO at this composition (blue dotted lines), where the MIT occurs on cooling below $T_{vt} \approx 135$ K and the resistivity becomes unmeasurably large below ~30 K. The exact position of T_{vt} is better determined by derivative analysis, such as the Zabrodskii plots in Figs. 1(c,d). These plot W *vs.* T on a ln-ln plot, where $W = -d\ln\rho/d\ln T$ is essentially a reduced activation energy [52]. On such plots, the MIT appears as a clear maximum (blue dotted lines in Figs. 1(c,d)), accurately determining T_{vt}. Moving to films, and starting with the high-t regime, Figs. 1(a,c) show the first striking result of this work. At t = 9 nm, identical behavior to our recent report [37] is observed, T_{vt} on these YAO substrates (-2.1% strain) being promoted to 245 K (the peak in the red curve in Fig. 1(c)). Data on cooling/warming (not shown here, see [37]) reveal weak hysteresis, confirming that the first-order nature of the bulk transition is retained. As t is increased to 35 nm, however, the MIT becomes increasingly smeared, as evident in both Figs. 1(a) and 1(c). At higher t,

surprising behavior then emerges, with clear evidence of *two* successive transitions. This is already visible in the 58 and 150 nm curves in Fig. 1(a), but becomes obvious in the high-t curves in Fig. 1(c), where a relatively sharp peak occurs near 245 K, along with a much broader peak at a lower T, the center of which decreases from 180 to ~100 K as t increases from 44 to 150 nm. The significance of these temperatures is readily apparent: 245 K is the fully-strained T_{vt} [37], while ~135 K corresponds to the bulk T_{vt} [25]. This immediately suggests coexistence of two film regions above $t_{crit} \approx 30$ nm, one with the fully-strained T_{vt} and one with close to bulk T_{vt}. This is clearly inconsistent with typical strain relaxation, where, above t_{crit}, the entire film would be expected to progressively strain relax [53–57], in stark contrast to coexistence of strained and near-fully-relaxed regions. While we focus in this paper on the t-dependent T_{vt}, and the strain relaxation that drives it, as an aside, note that the low-T resistivity also evolves interestingly with t; this is related to phase coexistence with the ferromagnetic metallic phase on the compressive side of the strain phase diagram, which will be the focus of later work.

Figs. 1(b,d) focus on the low-t regime, which also reveals intriguing behavior. In this case, decreasing t from 9 to 4 nm has only minimal impact, specifically a minor increase in the width of the MIT (best seen in Fig. 1(d)). Further decrease to 3 nm (~8 u.c.), however, induces a clear change, the MIT broadening substantially, leading to significantly increased ρ(300 K) (Figs. 1(b,d)). At t = 2 nm (~5 u.c.), the MIT is then broadened to the point that no clear signature remains, even in Fig. 1(d), resulting in insulating behavior in $\rho(T)$ at all T. In essence, the T-dependent MIT is progressively suppressed and broadened below t = 9 nm (particularly below 4 nm), but with no change in T_{vt} (see Fig. 1(d)), ultimately destroying the metallicity at 300 K. We note immediately that this is intriguing, as, at such a first-order transition, any t-dependent factor that would favor the low-T/low-cell-volume/low-spin/insulating phase over the high-T/high-cell-volume/finite-

spin/metallic phase (or *vice versa*) would naturally shift T_{vt}. If the low-T insulating phase were favored at low thickness, for example, this would drive up T_{vt} and eventually generate insulating behavior at 300 K. This is not what occurs in Figs. 1(b,d), however, where the onset of 300-K insulating behavior in the low-t limit is instead associated with smearing of the MIT, *i.e.*, lowering of the change in ρ at the transition, with no change in T_{vt}.

The key findings from Fig. 1 are distilled into the t dependence of four key parameters in Fig. 2: (a) T_{vt}, (b) ln$W$ at T_{vt} (*i.e.*, the height of the peaks in Figs. 1(c,d)), (c) the width (w_{vt}) of the transition (*i.e.*, the width of the peaks in Figs. 1(c,d)), and (d) ρ(300 K). The first three of these are obtained by fitting the peaks in Figs. 1(c,d) (see Supplemental Material Fig. S1 [58] for fits) to a skewed Gaussian [59]:

$$\ln W = a + b\exp(-\ln 2[\ln(1 + 2c[(\ln T - \ln T_{vt})/w_{vt}])/c]^2) \quad (1),$$

where a, b, and c are constants describing the peak height and asymmetry, T_{vt} is the valence transition temperature, and w_{vt} is the transition width. In the higher-t (≥ 9 nm) regime, Figs. 2(a-c) show the clear splitting of the single transition into two components above $t_{crit} \approx 30$ nm (vertical red dashed line), which we label as "strained" and "relaxed". Above t_{crit}, Fig. 2(a) shows the t independence of the fully-strained T_{vt} at 245 K, while the relaxed T_{vt} rapidly drops, eventually crossing the bulk value (135 K, horizontal black dashed line) at the highest t (note the break on the t-axis). Correspondingly, ln$W$ at T_{vt} abruptly drops across t_{crit}, followed by a more gradual decrease at higher t (Fig. 2(b)). As this occurs, w_{vt} remains low (*i.e.*, a sharp transition) for the fully-strained component, while w_{vt} is distinctly larger (broader transition) for the relaxed component (Fig. 2(c)). ρ(300 K) (Fig. 2(d)) remains essentially constant as all of this higher-t evolution takes place, *i.e.*, the high-T metallic state is unaffected. In terms of the low-t regime, Fig. 2(a) confirms that T_{vt} is entirely unaffected by thickness reduction, while the transition amplitude (Fig. 2(b)) and width

(Fig. 2(c)) rapidly decrease and increase, respectively. ρ(300 K) then correspondingly increases quickly below ~4 nm (~10 u.c.). These trends reflect the smearing of the MIT as t is decreased (Fig. 1(d)), eventually resulting in insulating behavior at 300 K (Fig. 1(b)).

III.B ANOMALOUS STRAIN RELAXATION: EXPERIMENTAL CHARACTERIZATION

To elucidate the origins of the key phenomena in Figs. 1 and 2, *i.e.*, the existence of two distinct transitions above t_{crit} and the suppression of the MIT with no change in T_{vt} below ~4 nm, we turn to t-dependent structural characterization. Shown in Fig. 3(a) are t-dependent specular HRXRD data around the YAO 002_{pc} (pc = pseudocubic) and PYCCO 002_{pc} reflections. As expected, at $t < t_{crit}$ (~30 nm) the film 002 reflections occur at identical values of Q_z (the z-component of the scattering wave vector (in substrate reciprocal lattice units)), consistent with fully-strained (compressive), pseudomorphic growth [37]. The only effect of reducing t in this regime is to broaden the primary peaks and progressively space the Laue fringes. At $t > t_{crit}$, however, the Laue fringes vanish, and the primary film peak clearly splits into two. The relative intensity of the peak at the fully-strained position gradually decreases with t, while the relative intensity at the higher Q_z position increases. The latter peaks correspond to reduced c-axis lattice parameters, as would be expected after strain relaxation of compressively-strained films. These issues are probed more directly in Figs. 3(b-d), which are asymmetric RSMs around the 013_{pc} reflections of YAO and PYCCO, at t = 9, 58, and 150 nm. At 9 nm (Fig. 3(b)) the behavior is as expected, the film and substrate reflections occurring at identical Q_y (the y-component of the scattering wave vector), confirming identical in-plane lattice parameters, *i.e.*, full strain [37]. The film peak at this t is heavily streaked along Q_z due to finite size. At t = 58 and 150 nm, however (Figs 3(c,d)), the film reflection is clearly split into *two* components, one fixed at the fully-strained position, while the

other rapidly shifts towards the expected bulk position (red ×) [37]. Consistent with Fig. 3(a), there is no gradual shift of a single peak (even an asymmetric one) from the fully-strained to fully-relaxed locations, but instead clear splitting into two lobes. This is in stark contrast to typical strain relaxation [53–57], indicating that even just above t_{crit}, a fully-strained film region coexists with a region with near-bulk lattice parameter.

The key results from Fig. 3 are summarized in Fig. 4, which shows the t dependence of (a) the c-axis lattice parameter, (b) the Scherrer length normalized by thickness (Λ/t), and (c) the relative intensities of the fully-strained (left axis) and relaxed (right axis) peaks. The values in Fig. 4(a) were determined from peak positions in Fig. 3(a), the values in Fig. 4(b) from application of the Scherrer equation to peak widths in Fig. 3(a), and the values in Fig. 4(c) from, *e.g.*, $I_{strained} = I_{strained,peak} / (I_{strained,peak} + I_{relaxed,peak})$, where the I values are respective intensities. The anomalous strain relaxation is readily apparent in Fig. 4. As t is increased above t_{crit} (vertical red dashed line), one peak remains at the fully-strained location while the other rapidly approaches the bulk position (Fig. 4(a)), both peaks broaden (shrinking Λ/t, Fig. 4(b)), and there is a gradual transfer of intensity from the fully-strained to relaxed peaks (Fig. 4(c)). These trends indicate that above t_{crit} these YAO/PYCCO films abruptly evolve to a situation where a fully-strained region (confirmed below to be near the interface with the substrate) coexists with a near-fully-relaxed region (confirmed below to be near the surface), further increase in t leading to growth of $I_{relaxed}$ relative to $I_{strained}$. Again, this is in clear contrast to standard strain relaxation involving a gradual evolution of a single film peak from the fully-strained to fully-relaxed positions [53–57,60–62], as observed in a wealth of heteroepitaxial perovskite oxides [63–68]. Most importantly, these data clearly show that the unusual splitting of the T-dependent MIT into two distinct transitions in Figs. 1 and 2 is rooted in the anomalous strain relaxation shown in Figs. 3 and 4.

To further probe this unusual strain relaxation, cross-sectional STEM imaging was performed on films with $t > t_{crit}$. Fig 5(a) shows a wide-field-of-view low-magnification HAADF image of a 58-nm-thick PYCCO film on YAO. The image is striking: a near-periodic array of dark-contrast regions appear as vertical stripes, beginning not at the film/substrate interface but instead at a specific depth in the film interior. The lateral period of these features averages to ~18 nm, corresponding perfectly to $a_{pc}/|\varepsilon_{xx}| = 18$ nm, where a_{pc} is the bulk pseudocubic lattice parameter (3.777 Å) and $|\varepsilon_{xx}|$ is the magnitude of the in-plane epitaxial strain (~2.1%). This suggests that the periodic features in Fig. 5(a) are edge dislocations with Burgers vector magnitude $|\underline{b}| = a_{pc}$, as confirmed by the higher-magnification images in Fig. 5(b). The main panel in Fig. 5(b) shows that edge dislocations are present in the center of the dark stripe regions, while the atomic-resolution image in the inset to Fig. 5(b) (from the red boxed region) yields $|\underline{b}| = 3.8$ Å. This is exactly as expected if the dislocation array in Figs. 5(a,b) enables full strain relaxation in the upper region of the film, consistent with the HRXRD findings from Figs. 3 and 4. In other words, half-planes of missing unit cells occur laterally every ~18 nm in the top region of the film. Also consistent with HRXRD, the lower region of the film appears fully-strained and nominally defect-free, with an apparently sharp interface with the YAO. These observations also explain Fig. 4(b), *i.e.*, that neither film component achieves the Λ expected of a single film coherent throughout its thickness. A more quantitative view of the evolution of the microstructure with depth is provided in Fig. 5(c), which shows the lateral variation of the HAADF intensity (averaged over 3-nm-wide bands) at distances from the substrate/film interface (d) of 3, 8, 15, 22, 31, 39, and 47 nm (as color-coded on the left of Fig. 5(b)). The HAADF line scans evolve from essentially flat for $d \leq 15$ nm, to clearly modulated with a lateral period of ~18 nm at the highest d, the intensity minima

corresponding to the dislocation half-planes. Significantly, the onset of modulation occurs around 22 nm, becoming clear at 31-39 nm, *i.e.*, close to 30 nm (*i.e.*, t_{crit}) from the substrate/film interface.

STEM-EDX analysis (Fig. 6) reveals that the strain-relaxing dislocation array in Fig. 5 is also associated with *chemical* modulation. A wide-scale view of this is provided in Fig. 6(a), which shows EDX elemental maps of Pr, Y, and Ca along with a corresponding HAADF image. The bottom region of the film is chemically homogeneous at this scale. As emphasized by the orange arrows, however, the periodic dislocation half-planes in the top region of the film are systematically poor in Pr and rich in Ca, indicating that Ca dopant ions segregate to the dislocations. This is quantified in Figs. 6(b,c), which show lateral line scans of the HAADF intensity, and Pr, Y, and Ca concentrations, at the depths labeled "1" and "2", respectively, in Fig. 6(a). At point "1" (the bottom, strained film region), the HAADF intensity and Pr, Y, and Ca concentrations are essentially uniform (Fig. 6(b)). At point "2", however (the top film region), the HAADF intensity systematically decreases around each dislocation half-plane (the vertical grey bands in Fig. 6(c)). Correspondingly, the Pr concentration drops periodically at these points, while the Ca concentration peaks. Fig. 6(d) illustrates this at the atomic level, where a clear region of dark contrast arises in the central region of the image, corresponding to the half-plane of missing unit cells. The red boxed region on the left in Fig. 6(d) is shown in the center panel at atomic resolution, the right panel (Fig 6(e)) illustrating the dip in HAADF intensity at the dislocation half-plane, with the associated minimum (maximum) in the Pr (Ca) concentration. In films with $t > t_{crit}$, this Ca enrichment near the dislocation half-planes must of course decrease the average Ca doping in the remainder of the film, potentially contributing to the highest-t decrease in T_{vt} (to below the bulk value) in Fig. 2(a), as T_{vt} decreases at sufficiently low x in these compounds [33]. The

associated inhomogeneity in Ca doping also explains the highest-t increase in w_{vt} in Fig. 2(c), *i.e.*, the transition broadening.

Some of the key thickness- and depth-dependent trends from HRXRD and STEM/EDX also manifest in GIXR, as shown in Figs. 7(a,b). Fig. 7(a) plots the specular X-ray reflectivity (R) from films with various t, scaled by the Fresnel reflectivity, as is common [60]. The latter is proportional to Q_z^{-4}, where Q_z is the z-component of the scattering wave vector. At t = 5 and 9 nm, RQ_z^4 is approximately flat above the critical angle, aside from the expected Kiessig oscillations, which decrease in spacing as t is increased. A clear change in behavior occurs at 30 nm ($\sim t_{crit}$) and above, however, where RQ_z^4 develops a prominent kink at $Q_z \approx 0.2$ Å^{-1}, and the amplitudes of the Kiessig fringes are significantly damped. Quantitatively, the red/black solid lines through the data in Fig. 7(a) show that the reflectivity below t_{crit} can be well-fit with a simple single-layer model. The resulting real and imaginary parts of the X-ray scattering length density (SLD) are shown *vs*. depth in Fig. 7(b), with the full set of model parameters shown in Supplemental Material Table S1 [58]. For t = 5, 9, and 25 nm, the fits are achieved with SLDs within 1-5% of the ideal bulk value for PYCCO (horizontal dashed lines in Fig. 7(b)), and interface/surface roughnesses below 0.5 nm, *i.e.*, the single-unit-cell level. Above t_{crit}, however, single-layer fits failed to reproduce the data, even qualitatively. Instead, a two-layer model was required (see Table S1 [58] for detailed parameters), resulting in the distinctly different depth profiles shown in Fig. 7(b). The essential differences in the higher t regime are: (*i*) a substantially rougher top surface, which the two-layer model accommodates (note the more gradual drop-off in SLD at the surface, and the associated parameters in Table S1 [58]); and (*ii*) monotonically increasing substrate-film roughness, possibly indicating increased interdiffusion (*e.g.*, of Y) at higher growth times. Most importantly, the top surface roughening we deduce is consistent with STEM images (*e.g.*, Fig. 5(a)), which show

periodic surface corrugation driven by the periodic dislocation array that forms at $t > t_{crit}$, also consistent with the loss of Laue fringes above t_{crit} in HRXRD (Fig. 3(a)).

A final piece of structural characterization is provided in Figs. 7(c-e), which show AFM images and analysis of films above and below t_{crit}. At t = 8 nm (Fig. 7(c)), flat terraces and unit-cell-high steps are found, yielding root-mean-square (RMS) roughness of only 0.15 nm, quite consistent with GIXR (Table S1 [58]). At $t \approx 150$ nm, however (*i.e.*, far above t_{crit}), island formation becomes clear in Fig. 7(d), generating a higher RMS roughness of 0.95 nm, and a lateral correlation length of 22 nm. This is in good agreement with both GIXR (Fig. 7(b), Table S1 [58]) and STEM (Fig. 5(a)), further confirming the corrugation of the top surface with a lateral period ~20 nm when $t > t_{crit}$, associated with the periodic dislocation array. The two AFM height (z) scans in Fig. 7(e), from the lines indicated by the arrows in Figs. 7(c,d), reinforce this point.

III.C ANOMALOUS STRAIN RELAXATION: DISCUSSION

The above transport and structural/chemical characterization data generate a clear picture of the strain relaxation in these compressively-strained YAO/PYCCO films. As the t_{crit} of ~30 nm is exceeded, almost immediately, a near-fully-relaxed upper film region coexists with a fully-strained lower region. The lower region is nominally chemically uniform and defect-free, while the upper region hosts a near-periodic array of dislocations that form in the film interior, relaxing strain and generating lateral modulations in chemical composition (primarily Pr/Ca doping) and surface roughness. As a first point in discussing this strain relaxation, it is instructive to highlight the key differences between these observations and the classic strain relaxation mechanism of Matthews and Blakeslee (MB) [53–55,57,62], as extensively referred to in the literature [61,63–66,68]. In the MB picture, sessile dislocations formed at the film-substrate interface in the initial stages of

growth become glissile at t_{crit}, once the resolved shear force exerted by the growing pseudomorphic film exceeds the line tension restraining dislocation motion [55]. Glide then occurs laterally, eventually generating a crisscross pattern of edge dislocations at the film-substrate interface, the density of which fully relaxes strain [55,57,62]. Vitally, in this mechanism, the dislocations thus reach the film/substrate interface, and strain relaxation is triggered throughout the entire film thickness, as observed in numerous heteroepitaxial oxides [69–74]. This is in stark contrast to our findings, as the dislocations in our YAO/PYCCO films form in the film interior (Figs. 5(a,b), 6(a), *etc*.), and completely distinct upper (relaxed) and lower (strained) regions emerge (from transport, HRXRD, STEM/EDX, GIXR, and AFM (Figs. 1-7)).

Notably, there exists a modification of the MB mechanism that allows for nucleation of dislocation loops from the growing film surface, particularly *via* heterogeneous nucleation if the film surface roughens or develops islands [55,75–78]. At first sight, this would appear to be a plausible mechanism for the nucleation of the dislocations we observe, particularly in light of the roughening seen in STEM (Fig. 5(a)), GIXR (Fig. 7(b), Table S1 [58]), and AFM (Fig. 7(c-e)). This model also predicts, however, that the dislocation loops, after formation, glide down to the film-substrate interface, thus relieving strain through the entire thickness [75,76]. This is therefore again in contrast with our observations; in our films some countervailing force must pin the dislocations in a horizontal plane near t_{crit} (as in Figs. 5(a,b) and 6(a)). Several other atypical strain relaxation mechanisms have also been documented in heteroepitaxial films of oxides such as perovskites, including mechanisms based on V_O-ordered stripes [48,49,69,79,80], Ruddlesden-Popper faults and similar planar defects [81–85], antiphase and out-of-phase boundaries [86], and different forms of (interfacial) dislocation arrays [69,70]. None of these defect types are detected in our YAO/PYCCO films, however, and thus these mechanisms are also incapable of explaining our

observations. In particular, the V_O ordering frequently encountered in perovskite cobaltite thin films [48,49,69,79,80] is not observed here [37]. One thing that is worth noting, however, is that we are aware of at least one potentially related observation in perovskites. Specifically, Catalan *et al*. [87] reported anomalous changes in the *T*-dependent MIT in $NdGaO_3$(001)/$NdNiO_3$ films at thicknesses exceeding a critical value, reminiscent of the behavior in Figs. 1 and 2 of this work. Their $NdNiO_3$ films at low *t* exhibited a single peak in $d\ln\rho/dT$ *vs*. *T* at the MIT, while films with *t* of 185–550 nm showed a second peak at a temperature closer to bulk [87], analogous to Figs. 1(c) and 2(a). Unfortunately, *t*-dependent structural characterization data for those films was not presented in this *t* range, although the authors did posit strain relaxation into two distinct film components to explain their transport data [87].

The other remarkable feature of the strain relaxation we observe in these YAO/PYCCO films is the associated lateral chemical modulation (Fig. 6). The first point to discuss in this context is that a variety of complex strain-mediated interactions between dislocations and impurity point defects are known in various materials. The Cottrell atmospheres forming in alloys where small (often interstitial) impurity atoms segregate around dislocation cores, thereby generating pinning effects, is a classic example [88,89]. Interestingly, at least one example of this phenomenon has been claimed in perovskite oxides ($PbZr_{1-x}Ti_xO_3$ [90]). A second point of comparison is encountered in epitaxial films of compound semiconductors (particularly III-V and II-VI semiconductors), where spatially varying strain, differing ionic/atomic radii, and differing ionic/atomic mobility can couple in complex ways, resulting in a spatially-periodic composition modulation that effectively relaxes (local) strain during film growth [91–94]. Related phenomena could conceivably be at work in YAO/PYCCO, with chemical segregation occurring to relieve stresses at the dislocation cores and half-planes, particularly given our 600 °C growth temperature and the only ~18 nm distance

between dislocations. However, our primary observation is of chemical segregation to the dislocation half-planes in the upper film region, on the tensile strain side of the dislocations, which is inconsistent with the smaller radius of Ca^{2+} *cf.* Pr^{3+}. Moreover, the difference in ionic radii between Pr^{3+} and Ca^{2+} is only ~2%, compared to ~9% for Pr^{3+} and Y^{3+} [95], suggesting that any segregation, to any region of the dislocations, would involve Y rather than Ca, counter to our observations. While larger mass and lower diffusivity of Y *vs*. Ca could play a role here, it is likely that the chemical segregation shown in Fig. 6 is thus at least partly charge-driven, rather than solely strain-driven, explaining the role for aliovalent Ca^{2+} over isovalent Y^{3+}. Segregation of charged dopant ions around dislocations is in fact known in heteroepitaxial perovskite oxides, as recently emphasized in dislocation-rich systems such as $BaSnO_3$ [96]. Finally, we note parenthetically that the temperature-dependent valence changes on Pr and Co ions have not yet taken place in the 300-K images in Fig. 6, and certainly not at the growth temperature, meaning that a role for the valence transition in this process is difficult to imagine.

Summarizing, the unusual thickness evolution of the transport behavior shown in Figs. 1 and 2 is clearly rooted in the anomalous strain relaxation documented in Figs. 3-7. Above t_{crit}, YAO/PYCCO films form a lower film region that is nominally chemically homogeneous and defect free. Atop this is an upper region in which a periodic array of edge dislocations occurs mid-film, relaxing strain and generating surface roughening and lateral segregation of Ca^{2+} to the dislocation half-planes. These phenomena cannot be simply explained by MB or modified-MB strain relaxation, wherein dislocations propagate to the substrate/film interface, or to the formation of other extended defects such as V_O-ordered stripes, which are not detected. Instead, some countervailing interaction must pin the strain-relaxation-enabling edge dislocations in a plane ~20 nm from the YAO/PYCCO interface (*e.g.*, Fig. 5(a)). The origin of this interaction is currently

unknown, although this phenomenon may well have been sporadically observed in other perovskite oxides (*e.g.*, [87]). We hope that this work stimulates additional research in this direction.

III.D ULTRATHIN-LIMIT BEHAVIOR

Finally, with the anomalous strain relaxation at high t discussed in full, we now return to the second striking observation from Figs. 1 and 2: the gradual suppression of the MIT at low t (particularly below ~ 4 nm (~10 u.c.)), with no change in T_{vt}. Deeper insight into the origin of this behavior is provided in Fig. 8, which compares the $\rho(T)$ (right axis) of 3- and 11-nm-thick films with corresponding measurements of the change in their c-axis lattice parameters (Δc, left axis) from T-dependent HRXRD. Consistent with Sec. I and our recent report [37], the t = 11 nm YAO/PYCCO film exhibits a large (~1.3%) c-axis contraction on cooling through T_{vt} (see the red dashed extrapolation lines), with T dependence mirroring $\rho(T)$. At t = 3 nm (8 u.c.), however, where the MIT is smeared substantially (Fig. 8, right axis), resulting in insulating behavior to 300 K, the magnitude of Δc across the structural/valence/spin-state/metal-insulator transition is distinctly reduced (Fig. 8, left axis). The collapse of the c-axis lattice parameter in fact decreases to <1%, but maintains a near-identical shape to the t = 11 nm case. The magnitude of the cell volume collapse across the transition is thus suppressed commensurately with the magnitude of the resistivity change at the MIT, but with no change in T_{vt}. We suspect that this trend continues to yet lower t, although probing this is challenging due to the difficulty of detecting small T-dependent peak position changes on highly broadened peaks (see the low-t data in Fig. 3(a)). As already noted, the unusual aspect to this behavior is that the transition is clearly profoundly impacted by t reduction, but with no impact on T_{vt} (Figs. 1(b,d) and Fig. 8). Typically, such

significant changes would be expected to energetically favor either the low-T (insulating) or high-T (metallic) phases, thereby shifting the temperature at which their free energy curves intersect, altering T_{vt}.

The first point to note in discussing the above is that literature precedent for such a phenomenon exists. In $SrTiO_3/La_{0.33}Sr_{0.67}FeO_3$ films, for example, the Verwey-type T-dependent MIT has been reported to be largely pinned at ~190 K, but to gradually evolve into featureless insulating $\rho(T)$ in the very-thin-film limit [97]. Perhaps the simplest idea to explain such behavior would be that increased defects and disorder in the ultrathin limit could drive electronic localization, generating insulating-like $\rho(T)$ at progressively higher T. Once insulating-like behavior exceeds T_{vt} (~245 K here), electronic transport could become far less sensitive to the structural/spin-state/valence transition, naturally explaining a reduction in the resistivity change across T_{vt}. In our case, however, Fig. 8 establishes that the change in c across T_{vt} commensurately decreases with the change in ρ across T_{vt}, indicating continued coupling between structure and transport at the lowest probed t. We propose that a key additional factor here is the symmetry matching between the YAO and PYCCO. Specifically, the substrate space group (*Pnma*) matches both the high-T and low-T film space group (both are *Pnma* in PYCCO, but with a volume collapse across T_{vt}). As established in ultrathin $NdNiO_3$, for example, such matching of the symmetry between the substrate and the low-T film structure is highly significant, essentially enabling a bulk-like transition [98]. Related to this, growth of VO_2 films on symmetry-mismatched substrates like Al_2O_3 and ZnO gives rise to interfacial transition layers with modified MIT behavior [99,100], quite unlike symmetry-matched VO_2 on TiO_2 [101,102]. In our case, we propose that symmetry matching is a key factor that enables a bulk-like T_{vt} to persist to low t. At the very lowest t, we then hypothesize that increased defects and disorder eventually broaden the phase coexistence region between the metallic and

insulating phases, smearing the transition both in structure (Fig. 8) and transport (Figs. 1(b,d) and Fig. 8). This disorder could arise from the increased influence of interface and surface roughness, as well as additional point defects such as V_O, all of which would be naturally expected in the very-low-*t* limit.

IV. SUMMARY

The results of a detailed thickness-dependent study of compressively-strained $YAlO_3$(101)/ $(Pr_{0.85}Y_{0.15})_{0.7}Ca_{0.3}CoO_{3-\delta}$(001) films have been presented, based primarily on transport, high-resolution X-ray diffraction, and cross-sectional transmission electron microscopy. This material serves as a model system for the strain control of Pr valence transitions. The results reveal an unusual thickness evolution of the temperature-dependent valence-driven structural-spin-state/metal-insulator transition in this system, which can be directly traced to anomalous strain relaxation. In essence, above the critical thickness, a periodic array of misfit dislocations occurs in the $(Pr_{0.85}Y_{0.15})_{0.7}Ca_{0.3}CoO_{3-\delta}$, not at the substrate/film interface, but instead in the film interior, accompanied by lateral modulations in chemical composition (particularly Ca doping). This results, even just above the critical thickness, in the coexistence of a fully-strained homogeneous lower film region with a near-fully-relaxed chemically-modulated upper region, establishing an unusual mode of strain relaxation, which we discussed in detail. In the low-thickness limit, the temperature-dependent structural/metal-insulator transition is seen to gradually vanish, with, strikingly, no change in transition temperature, which we ascribe to effects due to increased disorder in the ultrathin-film limit in the presence of symmetry matching between the film and substrate. These results significantly elucidate the thickness and strain effects in this new ambient-

temperature valence transition system, also exposing a new strain relaxation mechanism in perovskite oxides, of broad potential interest and relevance.

SUPPLEMENTAL MATERIAL

See the supplemental material for additional transport data analysis, and parameters extracted from GIXR fitting.

AUTHOR CONTRIBUTIONS

CL, JED, and VC conceived of the study. JED, VC, WMP, LF, AJ, and CK grew the films and performed the structural characterization, under the supervision of CL. JED performed the transport measurements and led the data analysis, under the supervision of CL. SG and KAM performed the electron microscopy and associated analysis. TRC contributed to the analysis of the GIXR data. JED and CL wrote the paper, with input from all authors.

ACKNOWLEDGMENTS

Work at the University of Minnesota (UMN) was primarily supported by the Department of Energy (DOE) through the UMN Center for Quantum Materials under DE-SC0016371. Electron microscopy by SG and KAM was supported by the National Science Foundation (NSF) through the UMN MRSEC under DMR-2011401. Parts of this work were carried out in the Characterization Facility, UMN, which receives partial support from the NSF through the MRSEC program. We thank Michael Fitzsimmons, Richard James, and Javier Garcia Barriocanal for productive discussions.

REFERENCES

[1] R. R. Heikes, R. C. Miller, and R. Mazelsky, *Magnetic and Electrical Anomalies in $LaCoO_3$*, Physica **30**, 1600 (1964).

[2] P. M. Raccah and J. B. Goodenough, *First-Order Localized-Electron ⇆ Collective-Electron Transition in $LaCoO_3$*, Phys. Rev. **155**, 932 (1967).

[3] M. A. Korotin, S. Yu. Ezhov, I. V. Solovyev, V. I. Anisimov, D. I. Khomskii, and G. A. Sawatzky, *Intermediate-Spin State and Properties of $LaCoO_3$*, Phys. Rev. B **54**, 5309 (1996).

[4] M. Imada, A. Fujimori, and Y. Tokura, *Metal-Insulator Transitions*, Rev. Mod. Phys. **70**, 1039 (1998).

[5] Z. Ropka and R. J. Radwanski, ^{5}D *Term Origin of the Excited Triplet in $LaCoO_3$*, Phys. Rev. B **67**, 172401 (2003).

[6] M.W. Haverkort, Z. Hu, J.C. Cezar, T. Burnus, H. Hartmann, M. Reuther, C. Zobel, T. Lorenz, A. Tanaka, N.B. Brookes et al., *Spin State Transition in $LaCoO_3$ Studied Using Soft X-Ray Absorption Spectroscopy and Magnetic Circular Dichroism*, Phys. Rev. Lett. **97**, 176405 (2006).

[7] A. Podlesnyak, S. Streule, J. Mesot, M. Medarde, E. Pomjakushina, K. Conder, A. Tanaka, M. W. Haverkort, and D. I. Khomskii, *Spin-State Transition in $LaCoO_3$: Direct Neutron Spectroscopic Evidence of Excited Magnetic States*, Phys. Rev. Lett. **97**, 247208 (2006).

[8] R. F. Klie, J. C. Zheng, Y. Zhu, M. Varela, J. Wu, and C. Leighton, *Direct Measurement of the Low-Temperature Spin-State Transition in $LaCoO_3$*, Phys. Rev. Lett. **99**, 047203 (2007).

[9] M. A. Señarís-Rodríguez and J. B. Goodenough, *Magnetic and Transport Properties of the System $La_{1-x}Sr_xCoO_{3-\delta}$ $(0 < x \leq 0.50)$*, J. Solid State Chem. **118**, 323 (1995).

[10] J. Wu and C. Leighton, *Glassy Ferromagnetism and Magnetic Phase Separation in $La_{1-x}Sr_xCoO_3$*, Phys. Rev. B **67**, 174408 (2003).

[11] P. P. Orth, D. Phelan, J. Zhao, H. Zheng, J. F. Mitchell, C. Leighton, and R. M. Fernandes, *Essential Role of Magnetic Frustration in the Phase Diagrams of Doped Cobaltites*, Phys. Rev. Mater. **6**, L071402 (2022).

[12] S. Tsubouchi, T. Kyômen, M. Itoh, P. Ganguly, M. Oguni, Y. Shimojo, Y. Morii, and Y. Ishii, *Simultaneous Metal-Insulator and Spin-State Transitions in $Pr_{0.5}Ca_{0.5}CoO_3$*, Phys. Rev. B **66**, 052418 (2002).

[13] S. Tsubouchi, T. Kyômen, M. Itoh, and M. Oguni, *Electric, Magnetic, and Calorimetric Properties and Phase Diagram of $Pr_{1-x}Ca_xCoO_3$ $(0 \leq x \leq 0.55)$*, Phys. Rev. B **69**, 144406 (2004).

[14] K. Knížek, J. Hejtmánek, P. Novák, and Z. Jirák, *Charge Transfer, Valence, and the Metal-Insulator Transition in $Pr_{0.5}Ca_{0.5}CoO_3$*, Phys. Rev. B **81**, 155113 (2010).

[15] J. L. García-Muñoz, C. Frontera, A. J. Barón-González, S. Valencia, J. Blasco, R. Feyerherm, E. Dudzik, R. Abrudan, and F. Radu, *Valence Transition in (Pr,Ca)CoO_3 Cobaltites: Charge Migration at the Metal-Insulator Transition*, Phys. Rev. B **84**, 045104 (2011).

[16] J. Herrero-Martín, J.L. García-Muñoz, S. Valencia, C. Frontera, J. Blasco, A.J. Barón-González, G. Subías, R. Abrudan, F. Radu, E. Dudzik, and R. Feyerherm, *Valence Change of Praseodymium in $Pr_{0.5}Ca_{0.5}CoO_3$ Investigated by x-Ray Absorption Spectroscopy*, Phys. Rev. B **84**, 115131 (2011).

[17] J. Herrero-Martín, J. L. García-Muñoz, K. Kvashnina, E. Gallo, G. Subías, J. A. Alonso, and A. J. Barón-González, *Spin-State Transition in $Pr_{0.5}Ca_{0.5}CoO_3$ Analyzed by x-Ray Absorption and Emission Spectroscopies*, Phys. Rev. B **86**, 125106 (2012).

[18] H. Masuda, T. Fujita, T. Miyashita, M. Soda, Y. Yasui, Y. Kobayashi, and M. Sato, *Transport and Magnetic Properties of $R_{1-x}A_xCoO_3$ (R = La, Pr and Nd; A = Ba, Sr and Ca)*, J. Phys. Soc. Jpn. **72**, 873 (2003).

[19] T. Fujita, T. Miyashita, Y. Yasui, Y. Kobayashi, M. Sato, E. Nishibori, M. Sakata, Y. Shimojo, N. Igawa, Y. Ishii et al., *Transport and Magnetic Studies on the Spin State Transition of $Pr_{1-x}Ca_xCoO_3$ up to High Pressure*, J. Phys. Soc. Jpn. **73**, 1987 (2004).

[20] J. Hejtmánek, E. Šantavá, K. Knížek, M. Maryško, Z. Jirák, T. Naito, H. Sasaki, and H. Fujishiro, *Metal-Insulator Transition and the Pr^{3+}/Pr^{4+} Valence Shift in $(Pr_{1-y}Y_y)_{0.7}Ca_{0.3}CoO_3$*, Phys. Rev. B **82**, 165107 (2010).

[21] H. Fujishiro, T. Naito, S. Ogawa, N. Yoshida, K. Nitta, J. Hejtmánek, K. Knížek, and Z. Jirák, *Valence Shift of Pr Ion from 3+ to 4+ in $(Pr_{1-y}Y_y)_{0.7}Ca_{0.3}CoO_3$ Estimated by X-Ray Absorption Spectroscopy*, J. Phys. Soc. Jpn. **81**, 064709 (2012).

[22] J. Hejtmánek, Z. Jirák, O. Kaman, K. Knížek, E. Šantavá, K. Nitta, T. Naito, and H. Fujishiro, *Phase Transition in $Pr_{0.5}Ca_{0.5}CoO_3$ and Related Cobaltites*, The European Physical Journal B **86**, 305 (2013).

[23] S. El-Khatib, S. Bose, C. He, J. Kuplic, M. Laver, J. A. Borchers, Q. Huang, J. W. Lynn, J. F. Mitchell, and C. Leighton, *Spontaneous Formation of an Exchange-Spring Composite via Magnetic Phase Separation in $Pr_{1-x}Ca_xCoO_3$*, Phys. Rev. B **82**, 100411(R) (2010).

[24] D. Phelan, Y. Suzuki, S. Wang, A. Huq, and C. Leighton, *Structural, Transport, and Magnetic Properties of Narrow Bandwidth $Nd_{1-x}Ca_xCoO_{3-\delta}$ and Comparisons to $Pr_{1-x}Ca_xCoO_{3-\delta}$*, Phys. Rev. B **88**, 075119 (2013).

[25] D. Phelan, K. P. Bhatti, M. Taylor, S. Wang, and C. Leighton, *Magnetically Inhomogeneous Ground State below the First-Order Valence Transition in $(Pr_{1-y}Y_y)_{0.7}Ca_{0.3}CoO_3$*, Phys. Rev. B **89**, 184427 (2014).

[26] J. B. Goodenough, *Localized to Itinerant Electronic Transition in Perovskite Oxides* (Springer-Verlag, Heidelberg, 2001).

[27] M. Topsakal, C. Leighton, and R. M. Wentzcovitch, *First-Principles Study of Crystal and Electronic Structure of Rare-Earth Cobaltites*, J. Appl. Phys. **119**, 244310 (2016).

[28] S. Cotton, *Lanthanide and Actinide Chemistry* (Wiley, Chichester, UK, 2006).

[29] R. Fehrenbacher and T. M. Rice, *Unusual Electronic Structure of $PrBa_2Cu_3O_7$*, Phys. Rev. Lett. **70**, 3471 (1993).

[30] M. Merz, N. Nücker, E. Pellegrin, P. Schweiss, S. Schuppler, M. Kielwein, M. Knupfer, M.S. Golden, J. Fink, C.T. Chen et al., *X-Ray Absorption Spectroscopy of Detwinned $Pr_xY_{1-x}Ba_2Cu_3O_{7-y}$ Single Crystals: Electronic Structure and Hole Distribution*, Phys. Rev. B **55**, 9160 (1997).

[31] C. Leighton, D.D. Stauffer, Q. Huang, Y. Ren, S. El-Khatib, M.A. Torija, J. Wu, J.W. Lynn, L. Wang, N.A. Frey et al., *Coupled Structural/Magnetocrystalline Anisotropy Transitions in the Doped Perovskite Cobaltite $Pr_{1-x}Sr_xCoO_3$*, Phys. Rev. B **79**, 214420 (2009).

[32] A. Jayaraman, V. Narayanamurti, E. Bucher, and R. G. Maines, *Continuous and Discontinuous Semiconductor-Metal Transition in Samarium Monochalcogenides under Pressure*, Phys. Rev. Lett. **25**, 1430 (1970).

[33] T. Fujita, S. Kawabata, M. Sato, N. Kurita, M. Hedo, and Y. Uwatoko, *On the Mechanism of the Spin State Transition of* $(Pr_{1-y}Sm_y)_{1-x}Ca_xCoO_3$, J. Phys. Soc. Jpn. **74**, 2294 (2005).
[34] T. Naito, H. Sasaki, and H. Fujishiro, *Simultaneous Metal–Insulator and Spin-State Transition in* $(Pr_{1-y}RE_y)_{1-x}Ca_xCoO_3$ *(RE=Nd, Sm, Gd, and Y)*, J. Phys. Soc. Jpn. **79**, 034710 (2010).
[35] H. Fujishiro, T. Naito, D. Takeda, N. Yoshida, T. Watanabe, K. Nitta, J. Hejtmánek, K. Knížek, and Z. Jirák, *Simultaneous Valence Shift of Pr and Tb Ions at the Spin-State Transition in* $(Pr_{1-y}Tb_y)_{0.7}Ca_{0.3}CoO_3$, Phys. Rev. B **87**, 155153 (2013).
[36] F. Guillou, Q. Zhang, Z. Hu, C. Y. Kuo, Y. Y. Chin, H. J. Lin, C. T. Chen, A. Tanaka, L. H. Tjeng, and V. Hardy, *Coupled Valence and Spin State Transition in* $(Pr_{0.7}Sm_{0.3})_{0.7}Ca_{0.3}CoO_3$, Phys. Rev. B **87**, 115114 (2013).
[37] V. Chaturvedi, S. Ghosh, D. Gautreau, W.M. Postiglione, J.E. Dewey, P. Quarterman, P.P. Balakrishnan, B.J. Kirby, H. Zhou, H. Cheng et al., *Room-Temperature Valence Transition in a Strain-Tuned Perovskite Oxide*, Nat. Commun. **13**, 7774 (2022).
[38] D. G. Schlom, L.-Q. Chen, C.-B. Eom, K. M. Rabe, S. K. Streiffer, and J.-M. Triscone, *Strain Tuning of Ferroelectric Thin Films*, Annu. Rev. Mater. Res. **37**, 589 (2007).
[39] D. G. Schlom, L.-Q. Chen, C. J. Fennie, V. Gopalan, D. A. Muller, X. Pan, R. Ramesh, and R. Uecker, *Elastic Strain Engineering of Ferroic Oxides*, MRS Bulletin **39**, 118 (2014).
[40] S. Middey, J. Chakhalian, P. Mahadevan, J. W. Freeland, A. J. Millis, and D. D. Sarma, *Physics of Ultrathin Films and Heterostructures of Rare-Earth Nickelates*, Annu. Rev. Mater. Res. **46**, 305 (2016).
[41] S. Catalano, M. Gibert, J. Fowlie, J. Íñiguez, J.-M. Triscone, and J. Kreisel, *Rare-Earth Nickelates* $RNiO_3$*: Thin Films and Heterostructures*, Rep. Prog. Phys. **81**, 046501 (2018).
[42] A. Bhattacharya and S. J. May, *Magnetic Oxide Heterostructures*, Annu. Rev. Mater. Res. **44**, 65 (2014).
[43] M. Huijben, L. W. Martin, Y.-H. Chu, M. B. Holcomb, P. Yu, G. Rijnders, D. H. A. Blank, and R. Ramesh, *Critical Thickness and Orbital Ordering in Ultrathin* $La_{0.7}Sr_{0.3}MnO_3$ *Films*, Phys. Rev. B **78**, 094413 (2008).
[44] M. A. Torija, M. Sharma, J. Gazquez, M. Varela, C. He, J. Schmitt, J. A. Borchers, M. Laver, S. El-Khatib, and C. Leighton, *Chemically Driven Nanoscopic Magnetic Phase Separation at the* $SrTiO_3(001)/La_{1-x}Sr_xCoO_3$ *Interface*, Adv. Mater. **23**, 2711 (2011).
[45] S. Stemmer and A. J. Millis, *Quantum Confinement in Oxide Quantum Wells*, MRS Bull. **38**, 1032 (2013).
[46] D. G. Schlom, L.-Q. Chen, X. Pan, A. Schmehl, and M. A. Zurbuchen, *A Thin Film Approach to Engineering Functionality into Oxides*, J. Am. Ceram. Soc. **91**, 2429 (2008).
[47] J. M. Rondinelli and N. A. Spaldin, *Structure and Properties of Functional Oxide Thin Films: Insights From Electronic-Structure Calculations*, Adv. Mater. **23**, 3363 (2011).
[48] J. Walter, S. Bose, M. Cabero, G. Yu, M. Greven, M. Varela, and C. Leighton, *Perpendicular Magnetic Anisotropy via Strain-Engineered Oxygen Vacancy Ordering in Epitaxial* $La_{1-x}Sr_xCoO_{3-\delta}$, Phys. Rev. Mater. **2**, 111404(R) (2018).
[49] J. Walter, S. Bose, M. Cabero, M. Varela, and C. Leighton, *Giant Anisotropic Magnetoresistance in Oxygen-Vacancy-Ordered Epitaxial* $La_{0.5}Sr_{0.5}CoO_{3-\delta}$ *Films*, Phys. Rev. Mater. **4**, 091401(R) (2020).
[50] V. Chaturvedi, W.M. Postiglione, R.D. Chakraborty, B. Yu, W. Tabiś, S. Hameed, N. Biniskos, A. Jacobson, Z. Zhang, H. Zhou et al., *Doping- and Strain-Dependent Electrolyte-*

Gate-Induced Perovskite to Brownmillerite Transformation in Epitaxial $La_{1-x}Sr_xCoO_{3-\delta}$ Films, ACS Appl. Mater. Interfaces **13**, 51205 (2021).
[51] M. Björck and G. Andersson, GenX*: An Extensible X-Ray Reflectivity Refinement Program Utilizing Differential Evolution*, J. Appl. Crystallogr. **40**, 1174 (2007).
[52] A. G. Zabrodskii, *The Coulomb Gap: The View of an Experimenter*, Philos. Mag. B **81**, 1131 (2001).
[53] J. W. Matthews and A. E. Blakeslee, *Defects in Epitaxial Multilayers: I. Misfit Dislocations*, J. Cryst. Growth **27**, 118 (1974).
[54] J. W. Matthews, *Coherent Interfaces and Misfit Dislocations*, in *Epitaxial Growth: Part B*, edited by J. W. Matthews (Academic Press, 1975), pp. 559–609.
[55] E. A. Fitzgerald, *Dislocations in Strained-Layer Epitaxy: Theory, Experiment, and Applications*, Mater. Sci. Rep. **7**, 87 (1991).
[56] D. J. Dunstan, S. Young, and R. H. Dixon, *Geometrical Theory of Critical Thickness and Relaxation in Strained‐layer Growth*, J. Appl. Phys. **70**, 3038 (1991).
[57] S. C. Jain, A. H. Harker, and R. A. Cowley, *Misfit Strain and Misfit Dislocations in Lattice Mismatched Epitaxial Layers and Other Systems*, Philos. Mag. A **75**, 1461 (1997).
[58] See the supplemental material at XXX for additional transport data analysis, and parameters extracted from GIXR fitting.
[59] R. D. B. Fraser and E. Suzuki, *Resolution of Overlapping Bands: Functions for Simulating Band Shapes*, Anal. Chem. **41**, 37 (1969).
[60] U. Pietsch, V. Holý, and T. Baumbach, *High-Resolution X-Ray Scattering*, 2nd ed. (Springer-Verlag, New York, 2004).
[61] J. S. Speck and W. Pompe, *Domain Configurations Due to Multiple Misfit Relaxation Mechanisms in Epitaxial Ferroelectric Thin Films. I. Theory*, J. Appl. Phys. **76**, 466 (1994).
[62] D. J. Dunstan, *Strain and Strain Relaxation in Semiconductors*, J. Mater. Sci.: Mater. Electron. **8**, 337 (1997).
[63] T. Suzuki, Y. Nishi, and M. Fujimoto, *Analysis of Misfit Relaxation in Heteroepitaxial $BaTiO_3$ Thin Films*, Philos. Mag. A **79**, 2461 (1999).
[64] T. Wang, K. Ganguly, P. Marshall, P. Xu, and B. Jalan, *Critical Thickness and Strain Relaxation in Molecular Beam Epitaxy-Grown $SrTiO_3$ Films*, Appl. Phys. Lett. **103**, 212904 (2013).
[65] S. Gariglio, N. Stucki, J.-M. Triscone, and G. Triscone, *Strain Relaxation and Critical Temperature in Epitaxial Ferroelectric $Pb(Zr_{0.20}Ti_{0.80})O_3$ Thin Films*, Appl. Phys. Lett. **90**, 202905 (2007).
[66] G. H. Lee, B. C. Shin, and I. S. Kim, *Critical Thickness of $BaTiO_3$ Film on $SrTiO_3$ (001) Evaluated by Reflection High-Energy Electron Diffraction*, Mater. Lett. **50**, 134 (2001).
[67] C. Merckling, M. El-Kazzi, G. Delhaye, V. Favre-Nicolin, Y. Robach, M. Gendry, G. Grenet, G. Saint-Girons, and G. Hollinger, *Strain Relaxation and Critical Thickness for Epitaxial $LaAlO_3$ Thin Films Grown on $SrTiO_3$(001) Substrates by Molecular Beam Epitaxy*, J. Cryst. Growth **306**, 47 (2007).
[68] A. Prakash, J. Dewey, H. Yun, J. S. Jeong, K. A. Mkhoyan, and B. Jalan, *Hybrid Molecular Beam Epitaxy for the Growth of Stoichiometric $BaSnO_3$*, J. Vac. Sci. Technol. A **33**, 060608 (2015).
[69] S. J. Pennycook, H. Zhou, M. F. Chisholm, A. Y. Borisevich, M. Varela, J. Gazquez, T. J. Pennycook, and J. Narayan, *Misfit Accommodation in Oxide Thin Film Heterostructures*, Acta Mater. **61**, 2725 (2013).

[70] B. P. Uberuaga, P. P. Dholabhai, G. Pilania, and A. Chen, *Semicoherent Oxide Heterointerfaces: Structure, Properties, and Implications*, APL Mater. **7**, 100904 (2019).
[71] F. Sánchez, M. V. García-Cuenca, C. Ferrater, M. Varela, G. Herranz, B. Martínez, and J. Fontcuberta, *Transition from Three- to Two-Dimensional Growth in Strained $SrRuO_3$ Films on $SrTiO_3(001)$*, Appl. Phys. Lett. **83**, 902 (2003).
[72] H. P. Sun, W. Tian, X. Q. Pan, J. H. Haeni, and D. G. Schlom, *Evolution of Dislocation Arrays in Epitaxial $BaTiO_3$ Thin Films Grown on (100) $SrTiO_3$*, Appl. Phys. Lett. **84**, 3298 (2004).
[73] J. Santiso, J. Roqueta, N. Bagués, C. Frontera, Z. Konstantinovic, Q. Lu, B. Yildiz, B. Martínez, A. Pomar, L. Balcells, and F. Sandiumenge, *Self-Arranged Misfit Dislocation Network Formation upon Strain Release in $La_{0.7}Sr_{0.3}MnO_3/LaAlO_3(100)$ Epitaxial Films under Compressive Strain*, ACS Appl. Mater. Interfaces **8**, 16823 (2016).
[74] H. Zhou, M. F. Chisholm, P. Pant, H. J. Chang, J. Gazquez, S. J. Pennycook, and J. Narayan, *Atomic Structure of Misfit Dislocations in Nonpolar ZnO/Al_2O_3 Heterostructures*, Appl. Phys. Lett. **97**, 121914 (2010).
[75] J. W. Matthews, *Defects Associated with the Accommodation of Misfit between Crystals*, J. Vac. Sci. Technol. **12**, 126 (1975).
[76] J. W. Matthews, A. E. Blakeslee, and S. Mader, *Use of Misfit Strain to Remove Dislocations from Epitaxial Thin Films*, Thin Solid Films **33**, 253 (1976).
[77] D. J. Eaglesham, E. P. Kvam, D. M. Maher, C. J. Humphreys, and J. C. Bean, *Dislocation Nucleation near the Critical Thickness in GeSi/Si Strained Layers*, Philos. Mag. A **59**, 1059 (1989).
[78] L. B. Freund, *Dislocation Mechanisms of Relaxation in Strained Epitaxial Films*, MRS Bull. **17**, 52 (1992).
[79] D. O. Klenov, W. Donner, B. Foran, and S. Stemmer, *Impact of Stress on Oxygen Vacancy Ordering in Epitaxial $(La_{0.5}Sr_{0.5})CoO_{3-\delta}$ Thin Films*, Appl. Phys. Lett. **82**, 3427 (2003).
[80] J. Gazquez, S. Bose, M. Sharma, M. A. Torija, S. J. Pennycook, C. Leighton, and M. Varela, *Lattice Mismatch Accommodation via Oxygen Vacancy Ordering in Epitaxial $La_{0.5}Sr_{0.5}CoO_{3-\delta}$ Thin Films*, APL Mater. **1**, 012105 (2013).
[81] T. Suzuki, Y. Nishi, and M. Fujimoto, *Defect Structure in Homoepitaxial Non-Stoichiometric Strontium Titanate Thin Films*, Philos. Mag. A **80**, 621 (2000).
[82] C. M. Brooks, L. F. Kourkoutis, T. Heeg, J. Schubert, D. A. Muller, and D. G. Schlom, *Growth of Homoepitaxial $SrTiO_3$ Thin Films by Molecular-Beam Epitaxy*, Appl. Phys. Lett. **94**, 162905 (2009).
[83] E. Breckenfeld, A. B. Shah, and L. W. Martin, *Strain Evolution in Non-Stoichiometric Heteroepitaxial Thin-Film Perovskites*, J. Mater. Chem. C **1**, 8052 (2013).
[84] W. Y. Wang, Y. L. Tang, Y. L. Zhu, J. Suriyaprakash, Y. B. Xu, Y. Liu, B. Gao, S.-W. Cheong, and X. L. Ma, *Atomic Mapping of Ruddlesden-Popper Faults in Transparent Conducting $BaSnO_3$-Based Thin Films*, Sci. Rep. **5**, 16097 (2015).
[85] H. Paik, Z. Chen, E. Lochocki, A. Seidner H., A. Verma, N. Tanen, J. Park, M. Uchida, S. Shang, B.-C. Zhou et al., *Adsorption-Controlled Growth of La-Doped $BaSnO_3$ by Molecular-Beam Epitaxy*, APL Mater. **5**, 116107 (2017).

[86] M.A. Zurbuchen, W. Tian, X.Q. Pan, D. Fong, S.K. Streiffer, M.E. Hawley, J. Lettieri, Y. Jia, G. Asayama, S.J. Fulk et al., *Morphology, Structure, and Nucleation of out-of-Phase Boundaries (OPBs) in Epitaxial Films of Layered Oxides*, J. Mater. Res. **22**, 1439 (2007).
[87] G. Catalan, R. M. Bowman, and J. M. Gregg, *Metal-Insulator Transitions in $NdNiO_3$ Thin Films*, Phys. Rev. B **62**, 7892 (2000).
[88] A. H. Cottrell and B. A. Bilby, *Dislocation Theory of Yielding and Strain Ageing of Iron*, Proc. Phys. Soc. A **62**, 49 (1949).
[89] M. A. Meyers and K. K. Chawla, *Mechanical Behavior of Materials*, 2nd ed. (Cambridge University Press, Cambridge, 2008).
[90] M. Arredondo, Q. M. Ramasse, M. Weyland, R. Mahjoub, I. Vrejoiu, D. Hesse, N. D. Browning, M. Alexe, P. Munroe, and V. Nagarajan, *Direct Evidence for Cation Non-Stoichiometry and Cottrell Atmospheres Around Dislocation Cores in Functional Oxide Interfaces*, Adv. Mater. **22**, 2430 (2010).
[91] J. M. Millunchick, R. D. Twesten, S. R. Lee, D. M. Follstaedt, E. D. Jones, S. P. Ahrenkiel, Y. Zhang, H. M. Cheong, and A. Mascarenhas, *Spontaneous Lateral Composition Modulation in III-V Semiconductor Alloys*, MRS Bull. **22**, 38 (1997).
[92] A. Zunger and S. Mahajan, *Atomic Ordering and Phase Separation in Epitaxial III-V Alloys*, in *Handbook on Semiconductors: Materials, Properties and Preparation*, Vol. 3b (Elsevier, Amsterdam, 1994), pp. 1399–1514.
[93] B. J. Spencer, P. W. Voorhees, and J. Tersoff, *Morphological Instability Theory for Strained Alloy Film Growth: The Effect of Compositional Stresses and Species-Dependent Surface Mobilities on Ripple Formation during Epitaxial Film Deposition*, Phys. Rev. B **64**, 235318 (2001).
[94] I. P. Ipatova, V. G. Malyshkin, A. A. Maradudin, V. A. Shchukin, and R. F. Wallis, *Kinetic Instability of Semiconductor Alloy Growth*, Phys. Rev. B **57**, 12968 (1998).
[95] R. D. Shannon, *Revised Effective Ionic Radii and Systematic Studies of Interatomic Distances in Halides and Chalcogenides*, Acta Cryst. A **32**, 751 (1976).
[96] H. Yun, A. Prakash, T. Birol, B. Jalan, and K. A. Mkhoyan, *Dopant Segregation Inside and Outside Dislocation Cores in Perovskite $BaSnO_3$ and Reconstruction of the Local Atomic and Electronic Structures*, Nano Lett. **21**, 4357 (2021).
[97] M. Minohara, M. Kitamura, H. Wadati, H. Nakao, R. Kumai, Y. Murakami, and H. Kumigashira, *Thickness-Dependent Physical Properties of $La_{1/3}Sr_{2/3}FeO_3$ Thin Films Grown on $SrTiO_3$ (001) and (111) Substrates*, J. Appl. Phys. **120**, 025303 (2016).
[98] J. Y. Zhang, H. Kim, E. Mikheev, A. J. Hauser, and S. Stemmer, *Key Role of Lattice Symmetry in the Metal-Insulator Transition of $NdNiO_3$ Films*, Sci. Rep. **6**, 23652 (2016).
[99] H. Zhou, M. F. Chisholm, T.-H. Yang, S. J. Pennycook, and J. Narayan, *Role of Interfacial Transition Layers in VO_2/Al_2O_3 Heterostructures*, J. Appl. Phys. **110**, 073515 (2011).
[100] F. J. Wong, Y. Zhou, and S. Ramanathan, *Epitaxial Variants of VO_2 Thin Films on Complex Oxide Single Crystal Substrates with 3*m *Surface Symmetry*, J. Cryst. Growth **364**, 74 (2013).
[101] N. F. Quackenbush, J.W. Tashman, J.A. Mundy, S. Sallis, H. Paik, R. Misra, J.A. Moyer, J.-H. Guo, D.A. Fischer, J.C. Woicik et al, *Nature of the Metal Insulator Transition in Ultrathin Epitaxial Vanadium Dioxide*, Nano Lett. **13**, 4857 (2013).
[102] H. Paik, J.A. Moyer, T. Spila, J.W. Tashman, J.A. Mundy, E. Freeman, N. Shukla, J.M. Lapano, R. Engel-Herbert, W. Zander et al., *Transport Properties of Ultra-Thin VO_2 Films*

on (001) TiO_2 Grown by Reactive Molecular-Beam Epitaxy, Appl. Phys. Lett. **107**, 163101 (2015).
[103] D. Fuchs, E. Arac, C. Pinta, S. Schuppler, R. Schneider, and H. v. Löhneysen, *Tuning the Magnetic Properties of $LaCoO_3$ Thin Films by Epitaxial Strain*, Phys. Rev. B **77**, 014434 (2008).
[104] V. Chaturvedi, J. Walter, A. Paul, A. Grutter, B. Kirby, J.S. Jeong, H. Zhou, Z. Zhang, B. Yu, M. Greven et al., *Strain-Induced Majority Carrier Inversion in Ferromagnetic Epitaxial $LaCoO_{3-\delta}$ Thin Films*, Phys. Rev. Mater. **4**, 034403 (2020).

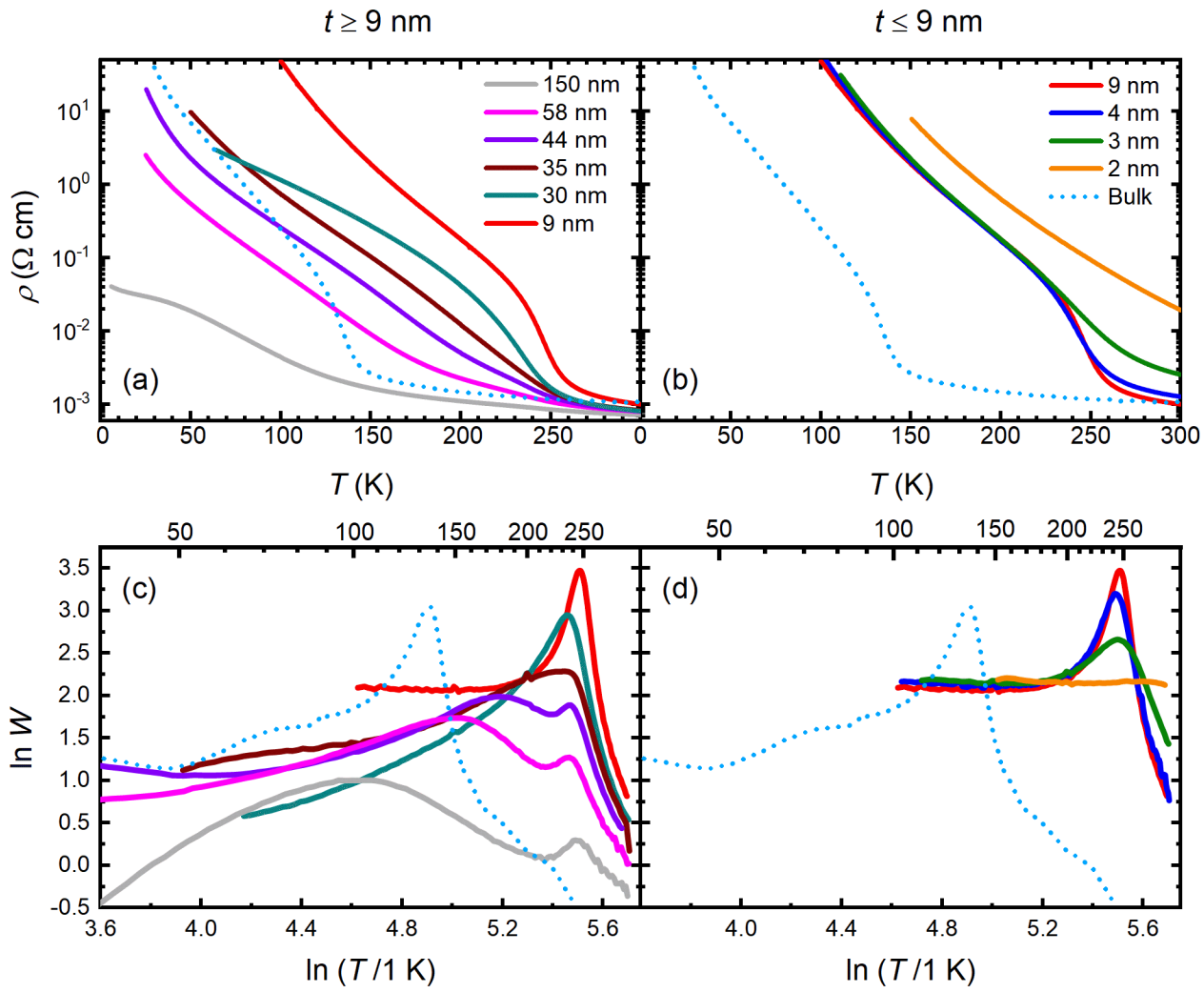

Figure 1: Temperature (T) dependence of the resistivity (ρ) (top panels, $\log_{10}$ scale, taken on warming) and corresponding Zabrodskii plots [52] (bottom panels, ln W *vs.* ln T, where, $W = -d\ln\rho/d\ln T$) of 2- to 150-nm-thick films. The data are divided into $t \geq 9$ nm (a,c) and $t \leq 9$ nm regimes (b,d) for clarity. A bulk polycrystalline sample of the same composition is shown for reference in all panels (blue dotted line).

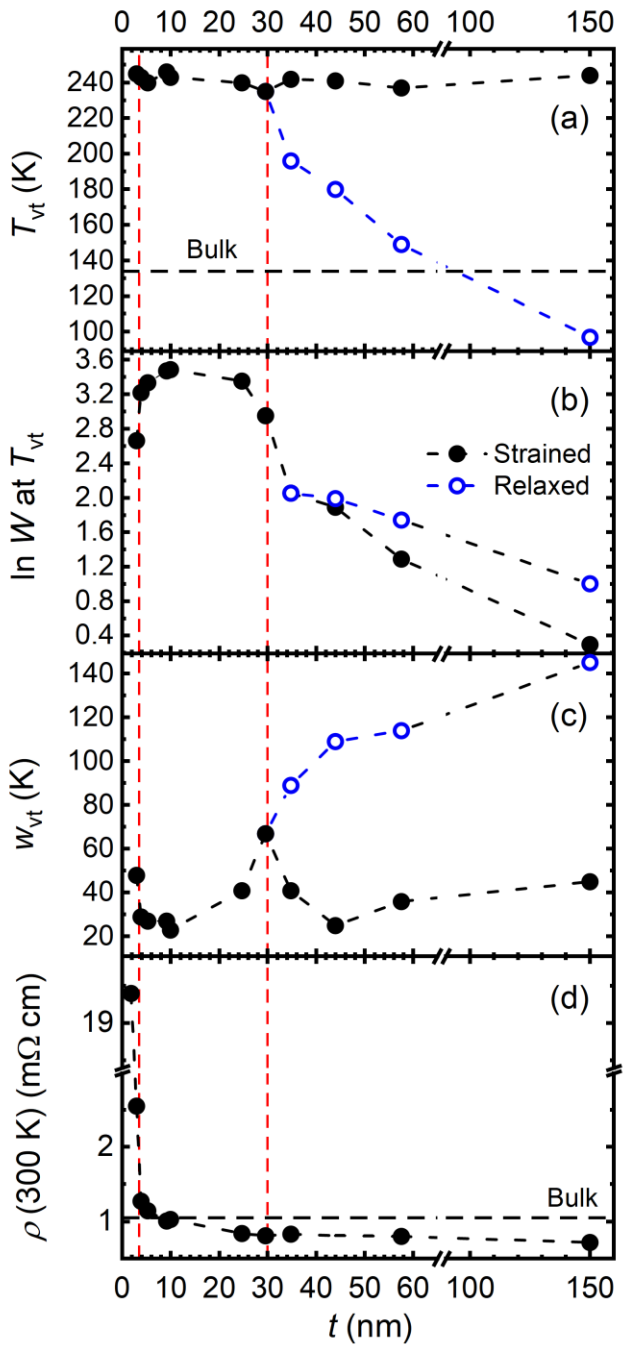

Figure 2: Thickness (t) dependence of (a) the transition temperature (T_{vt}), (b) the transition amplitude (ln W at T_{vt}, where $W = -d\ln\rho/d\ln T$), (c) the width of the transition (w_{vt}), and (d) the 300-K resistivity (ρ). As discussed in the text, T_{vt}, ln W at T_{vt}, and w_{vt} are determined by fitting skewed Gaussians to Zabrodskii plots (Figs. 1(c,d)). See Fig. S1 [58] for fits. In (a-c), black solid points and open blue points are for strained and relaxed components, respectively. Horizontal black dashed lines mark bulk polycrystalline values at this composition, while the vertical red dashed

lines mark the crossover to the ultrathin-limit (below ~3.5 nm) and the critical thickness for strain relaxation (~30 nm). Note the breaks on the t and ρ(300 K) axes.

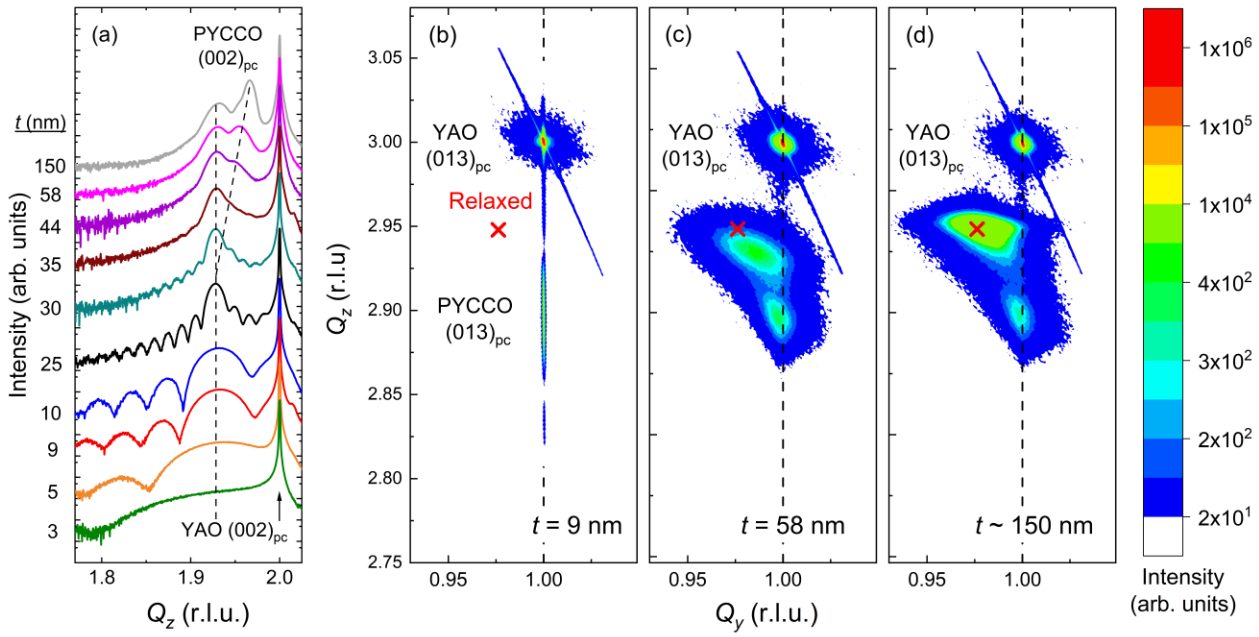

Figure 3: (a) Specular high-resolution X-ray diffraction scans around the pseudocubic 002 film and substrate peaks of 3- to 150-nm-thick films ($\log_{10}$ scale). The scans are vertically offset for clarity and labeled (left) with their thickness (*t*); substrate and film peaks are labeled. (b-d) Asymmetric X-ray reciprocal space maps around the pseudocubic 013 film peaks of 9-, 58-, and ~150-nm-thick films. In (a), black dashed lines are guides to the eye illustrating the strain relaxation with increasing thickness. In (b-d), bulk (relaxed) positions are marked with a red ×, while the vertical black dashed lines correspond to full strain, *i.e.*, pseudomorphic growth. In all cases, substrate (pseudocubic) reciprocal lattice units (r.l.u) are used.

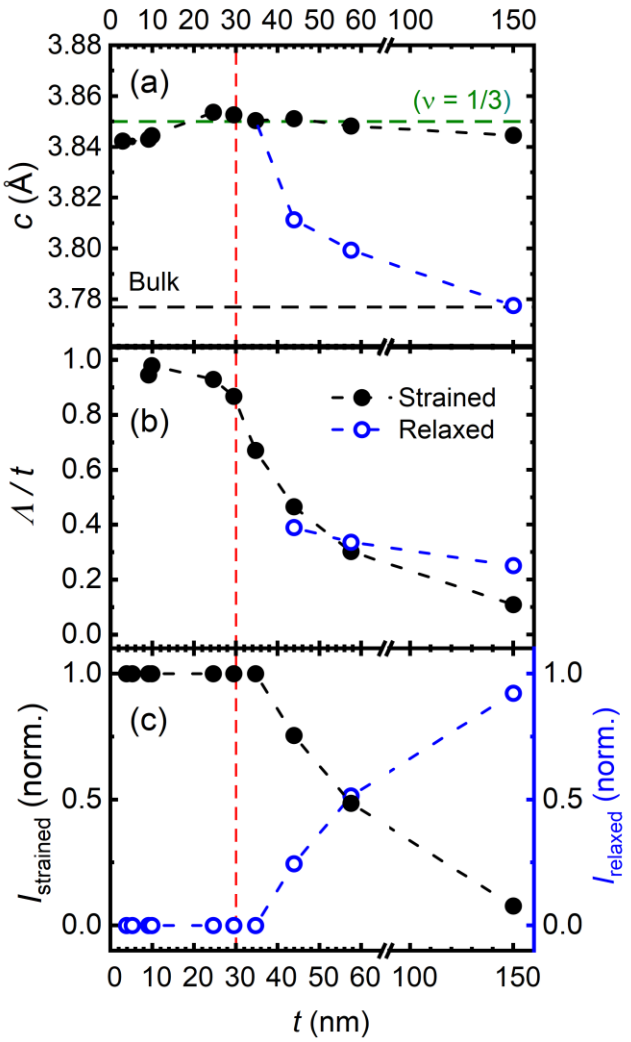

Figure 4: Thickness (t) dependence of (a) the out-of-plane lattice parameter (c), (b) the Scherrer length normalized to the thickness (Λ/t), and (c) the normalized X-ray diffraction intensities of the strained ($I_{strained}$, left axis) and relaxed ($I_{relaxed}$, right axis) components. In (a), the bulk polycrystalline value is shown as the horizontal black dashed line, while the green dashed line marks the expected fully-strained value based on a Poisson ratio (ν) of 1/3, as is typical in cobaltites [48,49,103,104]. In (c), the intensities are normalized to the sum of strained and relaxed peak intensities, *e.g.*, $I_{strained} = I_{strained,peak} / (I_{strained,peak} + I_{relaxed,peak})$. In all panels, black solid points and open blue points are for strained and relaxed components, respectively, and the vertical red dashed line marks the critical thickness for strain relaxation (~30 nm). Note the break on the t axis, as in Fig. 2.

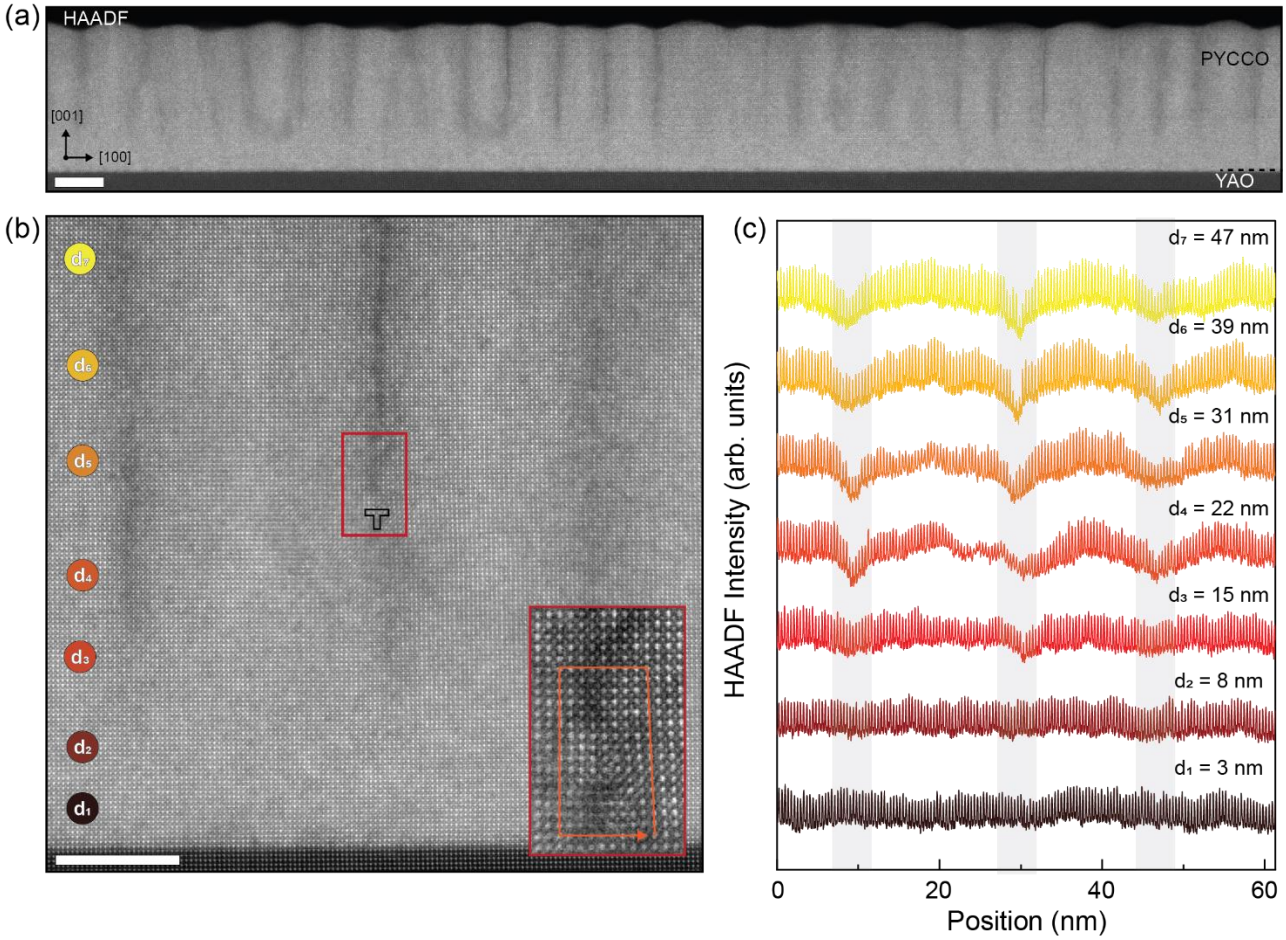

Figure 5: (a) Low-magnification high-angle annular dark field (HAADF) scanning transmission electron microscopy (STEM) image of a 58-nm-thick film in cross-section along [010]. Periodic HAADF intensity variations are observed in the top region of the film with an average lateral period of 18 nm. The scale bar is 20 nm. (b) Higher-magnification HAADF-STEM image of a section from (a), with an edge dislocation marked. The scale bar is 10 nm. Inset: Atomic-resolution image of the dislocation in (b), with a Burgers circuit shown (orange trace). (c) HAADF intensity lateral line scans across the film section in (b). The colors correspond to the distances from the film/substrate interface (*d*) shown in (b). The intensity was integrated over a band of height 3 nm.

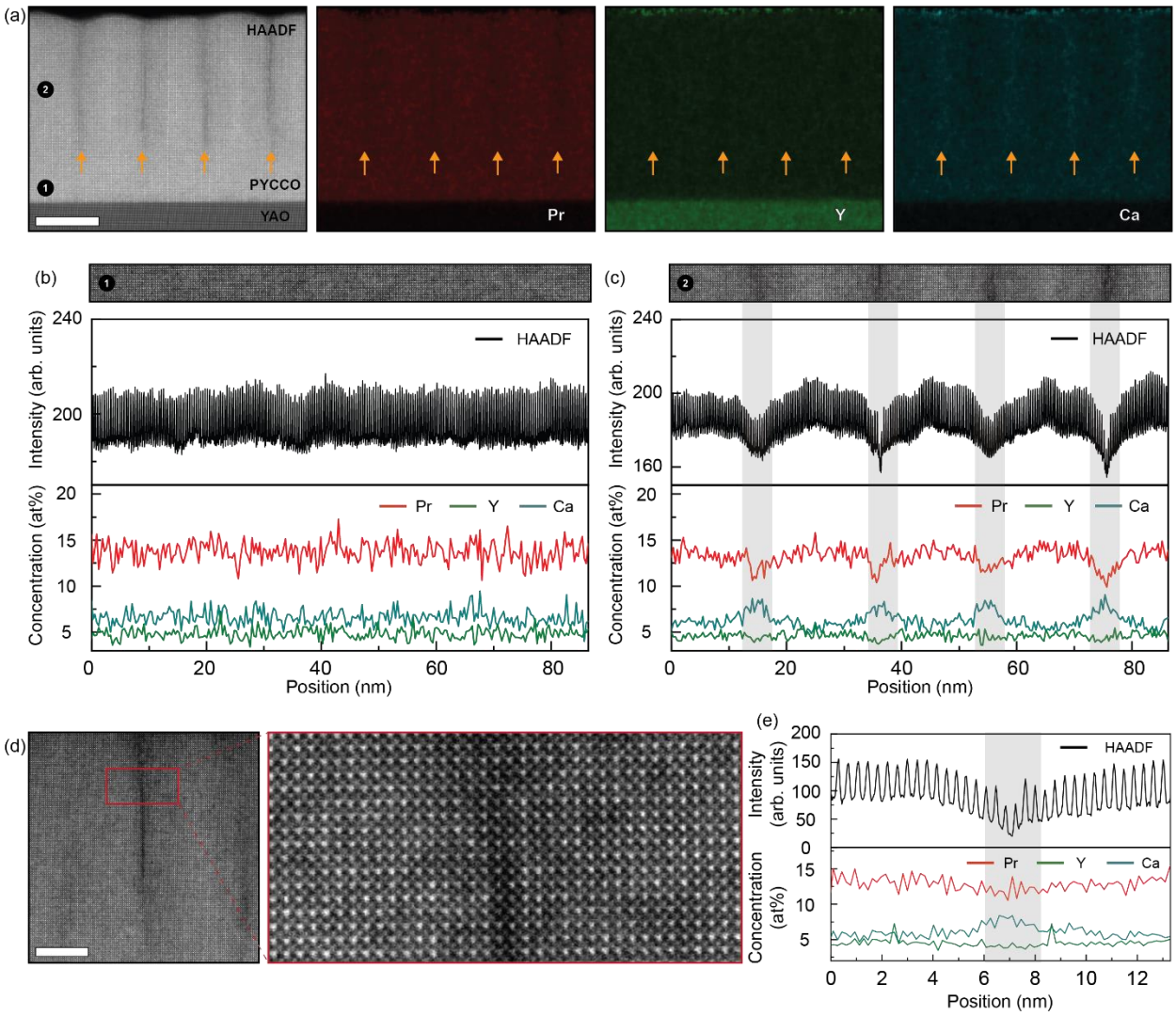

Figure 6: (a) Cross-sectional high-angle annular dark field (HAADF) image (along [010]), along with corresponding energy-dispersive X-ray spectroscopy (EDX) maps of the Pr, Y, and Ca concentration (atomic %), for the same film as in Fig. 5. Dislocations are labeled with orange arrows, and the scale bar is 20 nm. (b,c) Lateral line scans of HAADF intensity and Pr, Y, and Ca concentration (in atomic %) from the depths labeled "1" and "2" in panel (a). Intensities/concentrations were integrated over bands of height 6.8 nm in (b) and 10.5 nm in (c). (d) Atomic-resolution HAADF image (10-nm scale bar) focused on the area above a single dislocation (red boxed region). (e) Integrated HAADF intensity and corresponding lateral atomic % concentration profiles of Pr, Y, and Ca from the magnified panel in (d).

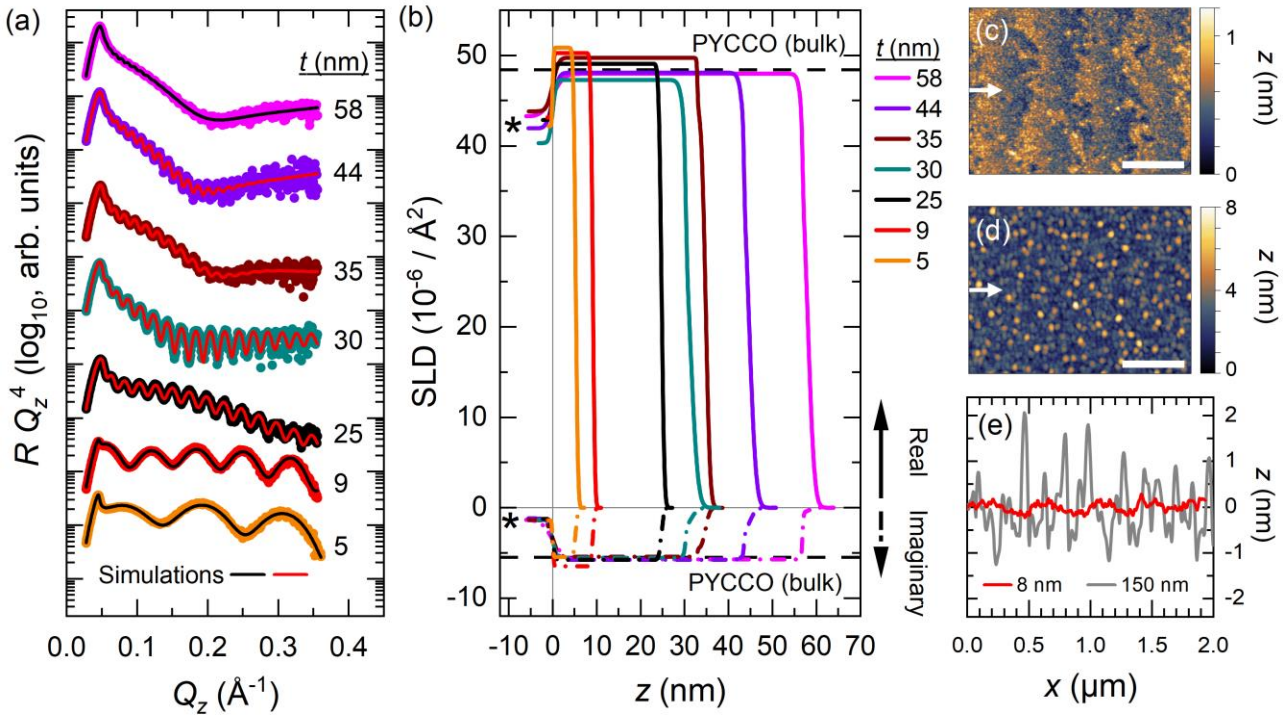

Figure 7: (a) Specular grazing-incidence X-ray reflectivity (R), normalized to the Fresnel reflectivity (which is proportional to Q_z^{-4}, where Q_z is the z-component of the scattering wave vector), for 5- to 58-nm-thick films (the thickness (t) is labeled to the right). Scans are vertically offset for clarity. Corresponding fits (red or black solid lines) are shown for all t. (b) Scattering length density (SLD) *vs.* depth (z), as refined from the X-ray reflectometry data in (a). Real and imaginary components of the SLD are shown on opposing (*i.e.*, positive and negative, respectively) vertical axes. Simulated SLD profiles for $t \leq 25$ nm (*i.e.*, below the critical thickness for strain relaxation) employ a single-layer model, while thicker films employ a two-layer model. The bulk real and imaginary SLD values for PYCCO are indicated by the black dashed horizontal lines, while the same bulk values for YAO are indicated by black stars. See Table S1 for all reflectometry fit parameters. (c,d) Atomic force microscopy images (2×1.5 μm^2) of a 8-nm-thick film (c) and a 150-nm-thick film (d). Scale bars are 500 nm. (e) Representative height (z) scans from AFM images, collected along lines indicated by white arrows in (c) and (d).

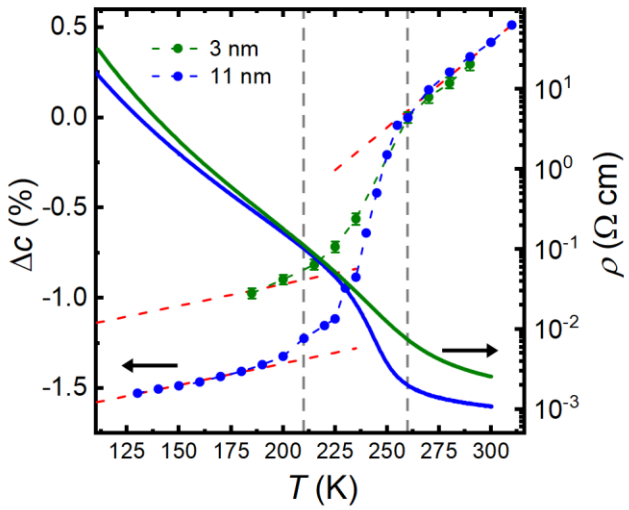

Figure 8: Temperature (*T*) dependence of the change in out-of-plane lattice parameter (Δ*c*) from the 260-K value (left axis), and the resistivity (ρ, right axis), of 3- and 11-nm-thick films. Error bars on Δ*c* for the 11-nm-thick film are smaller than the data points. Dashed lines are guides to the eye, indicating the approximate temperature bounds of the valence transition (gray) and the linear thermal expansion regimes above and below the transition (red).